Characterization on tensile behaviors of fracture process zone of nuclear graphite using a hybrid numerical and experimental approach

YX Tang[a], RKL Su[b], HN Chen[a*]

[a] Space Structures Research Center, Guizhou University, Guiyang, China
[b] Department of Civil Engineering, The University of Hong Kong, Hong Kong, China

Abstract

This paper reports an experimental and numerical study on the fracture properties of nuclear graphite NG-CT-01 produced in China. Three-point bending tests were performed on center-notch beams and electronic speckle pattern interferometry (ESPI) technique was employed to measure the full-field deformation of the beams. Besides, finite element analysis was performed by using extended finite element method to simulate the fracture behavior of graphite. Numerical results were compared with the experimental results and excellent agreement was obtained, validating the reliability and accuracy of the numerical model. Based on the strain field measured by ESPI technique, the formation and evolution of the fracture process zone (FPZ) in graphite were observed. The tension softening curve (TSC) of the graphite was determined by using a hybrid numerical and experimental approach. The influences of initial crack length to beam depth ratio on the fracture responses of graphite beam, including the load-displacement curves, double-K fracture parameters, TSCs and the length of the FPZ, were evaluated. In order to explain the correlation between the tension softening behaviors and the fracture mechanism of the FPZ, a tri-linear model was proposed. Furthermore, double-K fracture criterion was employed to predict the crack propagation in graphite.

*Corresponding author. E-mail: hqchen@gzu.edu.cn (Hongniao Chen)

Nomenclature

I, J, K	the sets of all nodes in the mesh, the nodes across the crack faces and the nodes near the crack tip
N_i	the shape function of node i
u_i	the nodal displacement of node i
a_i	the enriched nodal degree of freedom associated with Heaviside jump function
b_i^α	the enriched nodal degrees of freedom associated with asymptotic enrichment functions
r and θ	local polar coordinates defined at the crack tip
E	Young's modulus
L	length of beam
D	depth of beam
t	thickness of beam
S	span of beam
a_0	initial crack length
α_0	initial crack length to beam depth ratio
P	applied load
P_i	load at i^{th} step
P_c	peak load
P_{ini}	initial fracture load
δ_c	critical deflection at peak load
$CMOD_{ini}$	crack mouth opening displacement at initial fracture load
$CMOD_c$	critical crack mouth opening displacement at peak load
$CTOD_{ini}$	crack tip opening displacement at initial fracture load
$CTOD_c$	critical crack tip opening displacement at peak load
K_I	mode I fracture toughness
K_{Ic}^{ini}	initial fracture toughness
K_{Ic}^{un}	unstable fracture toughness
a_c	critical crack length at the peak
A_0	area under the load–deflection curve
G_F	fracture energy
$G_F^{P-\delta}$	fracture energy obtained from load-deflection curve
G_F^{TSC}	fracture energy obtained from tension softening curve
ε_{xx}	in-plane strain in the x direction
y	position of the main crack along the beam depth
σ	cohesive stress
w	crack opening width
w_c	critical crack opening width corresponding to zero cohesive stress
a	total crack length
Δa	extended crack length
l_{FPZ}	length of the FPZ

1. Introduction

Nuclear graphite is widely used as neutron moderators in High Temperature Gas-cooled Reactors (HTGRs). Meanwhile, graphite cores subject to different loads and effects as structural components. Under the effects of high temperature and fast neutron irradiation, there is a gradual damage accumulation in graphite, which leads to the changes of its dimensions and properties and the generation of internal stresses. The graphite may crack under the effects of the internal stresses and other mechanical loads [1], which will influence the structural integrity and threaten the safety of the HTGRs [2]. Therefore, the fracture properties of nuclear graphite are essential to the design and safety assessment of graphite members in the HTGRs.

Many efforts have been made in recent years to study the fracture characteristics of graphite materials. Heard et al. [3] observed the crack initiation and propagation of PGA graphite cylinders and confirmed that macro-crack followed an irregular path controlled by the direction of the applied tensile stress and the microstructure. Becker et al. [4] studied the crack initiation and propagation characteristics of two medium grained polygranular graphites, NBG10 graphite and GCMB grade graphite, and found the rising *R*-curve behavior was due to the formation of the fracture process zone (FPZ) and the increase in crack growth resistance was attributed to crack bridging and distributed microcracks. Su et al. [5] evaluated the tension softening curves in the FPZ of two nuclear graphites, the isotropic IG11 graphite and a Chinese NG-CT-01 graphite, by using an inverse displacement collocation method. Mostafavi et al. [6] observed the microcracks initiation and demonstrated the existence of the FPZ ahead of the crack tip by X-ray computed tomography measurement. They suggested

that simulation of the fracture of nuclear graphite requires a constitute model capable of showing softening behavior. Li et al. [7] examined the size effect on the fracture toughness of NBG-18 graphite by using an analytical model based on the FPZ near the crack tip and found it is size independent. Burchell et al. [8] determined the shear fracture toughness of PCEA and NBG-18 series. Chi [9] compared the fracture toughness and strain energy release rate of six nuclear graphite grades. Chen et al. [10] estimated the FPZ size of the isotropic IG11 graphite during the whole fracture process and found that the graphite material near the crack tip experienced biaxial tensile stress by observing the strain contours in the horizontal and vertical directions. Barhli et al. [11] confirmed that tension softening occurred in the FPZ by using in situ mapping of total and elastic strains within it. They pointed out that the elastic strain energy release rate around the crack tip field could be employed as a fracture propagation criterion for IM1-24 polygranular graphite. Tang et al. [12] pointed out that the existing formula based on linear elastic fracture mechanics (LEFM) is no longer applicable for the displacement calculation around the crack tip due to the presence of the FPZ. They established the relationship of crack opening displacement and crack length in the near-isotropic NG-CT-01 graphite beam under three-point bending by fitting the experimental data.

Previous studies indicate that the FPZ causes certain nonlinearity and quasi brittleness in the fracture behavior of graphite [6, 10, 12, 13] and better understanding of characteristics of the FPZ may increase confidence in structural integrity assessments [4]. Therefore, it is of significance to investigate the characteristics of the FPZ to understand the fracture behavior of graphite.

Research on the FPZ in quasi-brittle material usually focuses on its geometry and softening properties [14]. For geometric characteristic of the FPZ, this paper presents a direct observation of the FPZ in nuclear graphite by using electronic speckle pattern interferometry (ESPI) technique. Full-field deformation and crack evolution during the whole fracture process in graphite beam were measured. As the development of the FPZ, stiffness of the material is reduced and its ability to transfer stress is weakened. This phenomenon can be regarded as softening behavior of quasi-brittle material and defined mathematically by the tension softening curve (TSC), which represents the relationship between the cohesive stress σ and crack opening width w [15].

Since it is difficult to make an accurate estimation of the TSC from a uniaxial tension test, the TSC of graphite has been indirectly estimated by the incremental displacement collocation method (IDCM) [5]. This method is capable of evaluating the TSC in a step-by-step manner and does not need a prior assumption on the shape of TSC. Comparing with other inverse analysis methods, ill-conditioned problems can be eliminated because the IDCM considers both the global and local responses of the specimen in the displacement collocation. Besides, the TSC estimated by the IDCM satisfies the displacement requirements over the complete fracture process [16]. Due to these advantages, the IDCM has been applied to determine the TSCs of various quasi-brittle materials, including mortar [16], graphite [5], and concrete [14]. However, in order to employ the IDCM, local deformation in the FPZ needs to be measured with high accuracy, which requires the assistance of advanced techniques, such as the ESPI [5], X-rays tomography [11, 17], acoustic emission [7], digital image correlation technology [18], synchrotron X-ray and neutron diffraction [19]. In the

case of limited laboratory conditions, the application of the IDCM will be restricted.

In order to overcome the limitations of measurement resolution, numerical simulation based on extended finite element method (XFEM) is used to obtain the local response of graphite and a hybrid approach, specifically combined XFEM and IDCM, is introduced to determine the TSC of graphite. The XFEM has emerged as a powerful numerical method for the analysis of discontinuity problems, such as holes, inclusions and a crack [20, 21], and can overcome the inherent drawbacks of the traditional finite element (FE) methods by making the geometric modeling of crack independent of mesh and avoiding the need of re-meshing as the crack propagates [20, 21]. Therefore, the XFEM has been used to model crack propagation of quasi-brittle materials [10, 22, 23] and can provide local responses for the estimation of the TSC by using the IDCM in this study. Furthermore, as the relationship between the tension softening properties and fracture mechanism of the FPZ, which is conductive to clarify the effect of the FPZ in the fracture behavior of graphite, keeps unclear, this paper links the geometrical characteristic of the FPZ observed by using ESPI technique with the softening characteristic estimated by the combined XFEM-IDCM.

2. Theoretical background

2.1. XFEM

Within the framework of the XFEM, the displacement approximation consists of two parts, continuous and discontinuous, respectively. The continuous displacement is approximated by the classical FE method, and the discontinuity is characterized by additional enrichment functions, consisting of the Heaviside function to present the jump in displacements and the asymptotic functions to capture the singularity of stresses around the

crack tip in two-dimensional crack modeling [23]. The approximation displacement fields for

crack modeling in the XFEM are written in a general form as follows [20, 21]:

$$u(x) = \sum_{i \in I} N_i(x)u_i + \sum_{i \in J} N_i(x)H(x)a_i + \sum_{i \in K} N_i(x)(\sum_{\alpha=1}^{4} F_\alpha(x)b_i^\alpha) \tag{1}$$

in which *I*, *J*, and *K* are the sets of all nodes in the mesh, the nodes across the crack faces

(marked with squares in Fig. 1) and the nodes near the crack tip (marked with circles in Fig.

1), respectively. $N_i(x)$ and u_i are the shape functions and the nodal displacement of node *i*.

a_i is the enriched nodal degree of freedom associated with Heaviside jump function $H(x)$,

which takes a value of 1 on the positive side of the crack and -1 on the negative side of the

crack. b_i^α are the enriched nodal degrees of freedom associated with asymptotic

enrichment functions $F_\alpha(x)$, which are defined as follows [23]:

$$F_\alpha(x) = \sqrt{r}\left[\sin\frac{\theta}{2}, \cos\frac{\theta}{2}, \sin\theta\sin\frac{\theta}{2}, \cos\theta\sin\frac{\theta}{2}\right] \quad (\alpha=1,2,3,4) \tag{2}$$

in which *r* and θ are local polar coordinates defined at the crack tip.
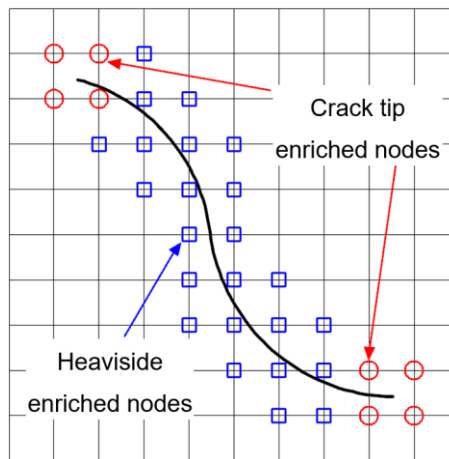

Fig. 1   The computational mesh with an arbitrary crack.

2.2. The combined XFEM and IDCM

Detailed computational procedures of the IDCM can be found in References [5, 14,

16]. Firstly, the displacements are measured and the tensile strength and elastic modulus are

estimated; then, the length of the FPZ is determined from the COD curve and the cohesive stresses in the FPZ are calculated; After that, the nodal cohesive stress are input into the FEM and the numerical displacements at the collocation points are computed. Once the cohesive stress at one loading step is determined by minimizing the discrepancy between the calculated and measured displacements, above procedures will be performed to the next loading step until the cohesive stress at the initial notch tip reduces to zero. In this step-by-step manner, the fully-developed TSC can be constructed by using the IDCM.

In the IDCM, both the global and local responses are employed to determine the TSC of quasi-brittle materials. The global responses, such as deflection (δ) and crack mouth opening displacement (CMOD), can be obtained easily from the experimental tests. However, the local responses, including the complete COD profile, the location of crack tip and the FPZ length at each analysis steps, can only be measured by using the measurement techniques with high resolution and are difficult to be obtained under ordinary laboratory conditions if not impossible.

In the combined XFEM-IDCM, three-point bending test is first simulated by using the XFEM and the reliability of the numerical simulation is calibrated by comparing the global displacements obtained from experiment and numerical simulation respectively. Furthermore, the simulated displacements at each of analysis steps, including δ, CMOD, crack opening tip displacement (CTOD) and crack opening displacement (COD) profile, are extracted to provide data input for the IDCM to evaluate the TSC of graphite.

In order to provide more boundary conditions for the inverse analysis and eliminating the individual differences of the samples, Young's modulus E can be estimated from the

measured initial compliance C_i of P-CMOD curve as follows [24]:

$$E = \frac{6Sa_0V_1(\alpha_0)}{C_iD^2t} \tag{3}$$

for span-depth ratio $S/D = 4$, the function $V_1(\alpha_0)$ can be expressed as

$$V_1(\alpha_0) = 0.76 - 2.28\alpha_0 + 3.87\alpha_0^2 - 2.04\alpha_0^3 + 0.66/(1-\alpha_0)^2 \tag{4}$$

in which a_0 is the initial crack length, $\alpha_0 (= a_0/D)$ is the initial crack length to beam depth ratio and t is the beam thickness.

3. Experiments and numerical simulation

3.1. Specimens and experimental setup

Experimental tests on center-notched beams were performed to study the fracture properties of NG-CT-01 graphite manufactured in China. The NG-CT-01 Series uses a small grain size and is manufactured by isostatic pressing. It therefore exhibits near isotropy. The grain size of the graphite was about 25 μm and the Poisson's ratio was taken as 0.14. The Young's modulus, compressive strength and tensile strength were found to be 10 GPa, 76MPa and 24 MPa, respectively. More details on the material properties of NG-CT-01 from the provider can be found in Reference [5]. Beam dimensions ($L \times D \times t$) were 220 mm × 50 mm × 25 mm and the beam span S was 200 mm. A center notch was cut for each beam by a saw. The notch depth and width were 20 mm and 0.3 ± 0.02 mm, respectively. The samples were placed in the air and the relative humidity of the laboratory is about 75% – 85%.

Using an MTS and bend fixture, three-point bending tests were performed and the experimental setup is shown in Fig. 2a. The actuator was moved upward to load the beam by using the displacement control with a loading rate of 0.01 mm/min. The CMOD was

measured by a clip gauge installed at the end of the initial notch, and the mid-span deflection δ were measured by the LVDTs, as shown in Fig. 2b. By using a closed-loop servo hydraulic system, the crack growth was well controlled and the complete load-displacement curves were recorded by a data logger.
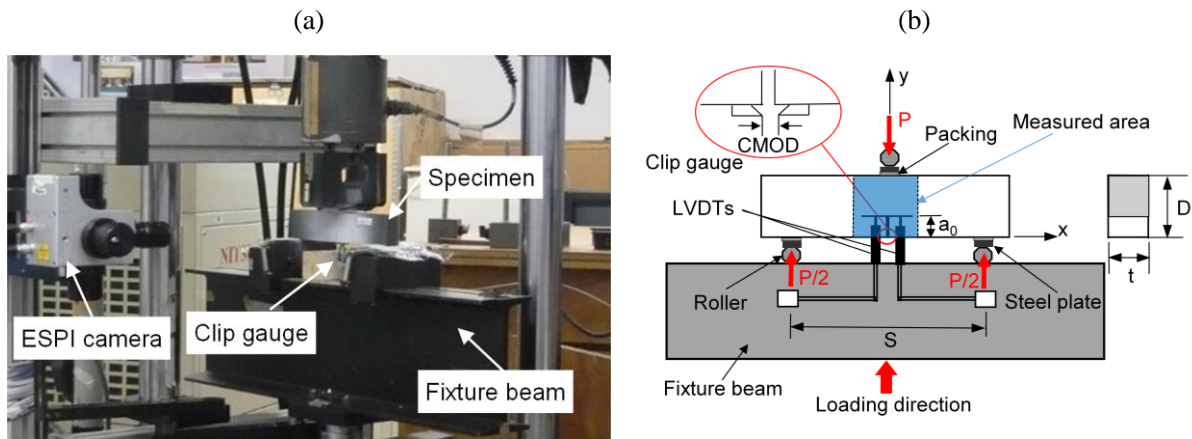
(a)　　　　　　　　　　　　　　　　(b)

Fig. 2　Three-point bend test: (a) experimental setup; (b) schematic view.

The surface deformation near the mid-span of the specimens was measured by a 3D ESPI system (Q300 produced by Dantec-Ettemeyer). The measured zone was about 100 mm (horizontal) × 70 mm (vertical), the illumination arm was 70 mm, the laser wavelength was 785 nm, and the object distance was approximately 380-385 mm. In the present setup, the measurement accuracy of ESPI achieved approximately 0.2 μm. The speckle pattern which reflects the interference of the laser scattered from the measuring surface, was captured by the ESPI sensor at each record step. By using a post-processing software ISTRA [25], the raw data was converted into in-plane displacement fields. More details on the principle of ESPI measurement can be found in References [5, 10, 26].

3.2. XFEM simulation

Using a commercial finite element software ABAQUS 6.14 coupled with XFEM, the graphite beam subjected to three-point bending was simulated. Numerical model with a

total of 7918 two-dimensional four-node plane-stress solid elements (CPS4R) was built, as shown in Fig. 3. The mesh size near the central notch was 0.5 mm and the mesh size outside the crack propagation domain was 5 mm. The left support was constrained in both x and y directions while the right support was constrained only in y direction. A coupling constraint was applied and vertical downward displacement was added at the constraint control point to provide a displacement loading mode.
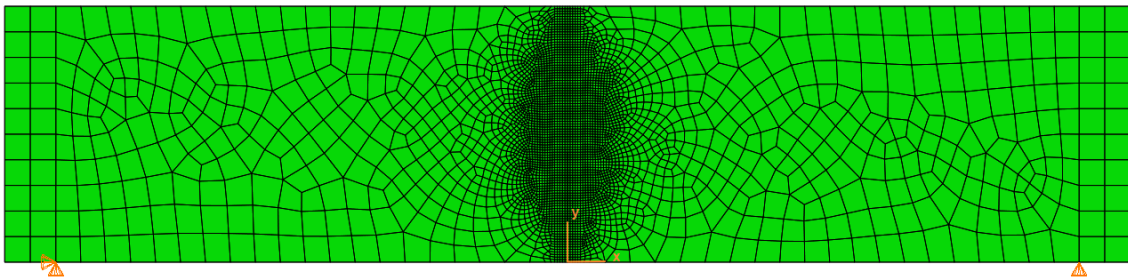

Fig. 3   Finite element model of three-point bending beam.

The bulk material was assumed to be homogeneous and its properties were the same as those measured in previous experiment. The maximum principal stress criterion (MAXPS) was employed as the cracking initiation criterion. The crack propagation direction was perpendicular to the direction of the maximum principal tensile stress, which was equal to 24 MPa. The energy-based linear softening constitutive relation was used to characterize the softening behavior of the FPZ. The fracture energy obtained from the tests was 175 N/m and the coefficient of damage stabilization was 2×10^{-5}.

4. Experimental and XFEM simulation results

4.1. Load-displacement curves

The load-deflection (P-δ) and load-CMOD (P-CMOD) curves of the center-notched beams during the entire loading process are presented in Fig. 4a and Fig. 4b, respectively. Good agreements were found by comparing the experimental and numerical results,

demonstrating the feasibility and accuracy of the XFEM simulation. It can also be observed

that the *P*-CMOD curves of different samples present more consistency than the *P*-*δ* curves,

which can be interpreted that the inevitable vertical gaps between the specimen and the

supports during the tests cause measuring errors in the deflection [12, 27].
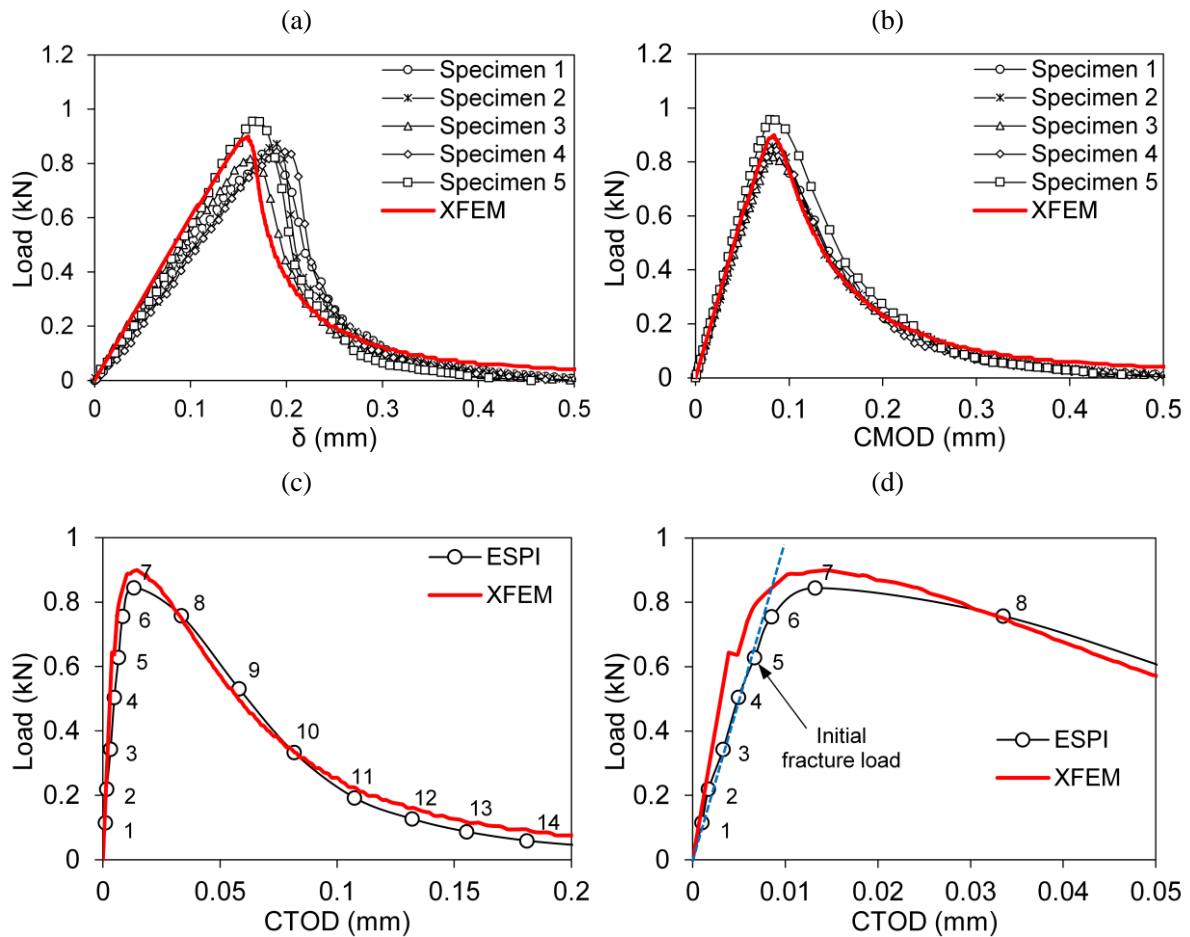

Fig. 4   Load-displacement curves: (a) *P*-*δ* curves; (b) *P*-CMOD curves; (c) *P*-CTOD curves; (d) locally

magnified *P*-CTOD curves.

The crack tip opening displacement (CTOD) can be determined from the relative

displacement in the *x*-direction at the notch tip (*y* = 20 mm in this study) [28]. Taking

Sample 1 as example, the load versus CTOD (*P*-CTOD) curves obtained from ESPI and

XFEM simulation are shown in Fig. 4c. A satisfactory agreement between the experimental

and numerical results can also be observed. Similar with the discovery in IG11 graphite

[10], the CTOD increased linearly with the load at the initial loading stage and the slope of the P-CTOD curve was reduced accordingly when the load increased to a certain level, as shown in the locally magnified curves in Fig. 4d. The end points of the linear segments of P-CTOD curve was regarded as the onset point of stable crack propagation and the corresponding load was denoted as the initial fracture load P_{ini} [29], which was approximately 0.637 kN for this specimen. The numerical curve also shows that there is an abrupt increase in displacement at the initial fracture load. It is worth noting that the CTOD was not equal to zero when a crack initiated from the tip of the notch, which may be due to the initiation and localization of microcracks ahead of the notch tip [30].

4.2. Observations of the crack evolution

Due to the formation and propagation of the FPZ, graphite exhibits some non-linearity during fracture process. Therefore, it is necessary to investigate the properties of crack growth. In previous studies [4, 10, 14], the interference fringe patterns and wrapped phase maps were employed to observe the crack evolution, which could only provide a qualitative description of the development of the FPZ rather than a quantitative assessment. To gain further investigation on the crack propagation, in-plane strain contour will be analyzed [4, 11] and the region of the FPZ can be defined by strain.

3D strain profiles in the x direction (ε_{xx}) of Sample 1 at the peak load are plotted in Fig. 5. It can be observed that strain peak occurs around the notch, which can be considered as cracking region. It can be seen that the closer to the crack front, the slighter the local strain peak was. It should be noted that the strain is simply caused by discontinuity of the crack displacement field and its magnitude depends on the crack opening and the ESPI

measurement parameters (i.e. distance of the gauge length), thus special attentions should be paid to comparisons with real strains of the material. However, the use of a criterion that is smaller than the tensile failure strain of graphite is sensible for defining a minimum extent of the FPZ.

The crack tip can be identified at the position where the COD is zero, which is approximately 25 mm along the y direction as illustrated in Fig.7. From the locally magnified strain distribution along the x direction, it can be found that the maximum strain occurs near the notch and is approximately 0.75×10^{-3} at the crack tip, which is close to a third of the maximum tensile strain 2.4×10^{-3} calculated from the tensile strength and Young's modulus. Similar finding was reported by Becker et al. [4] who indicated that the material might have some damage caused by microcracks [3] when it underwent more than a third of the maximum tensile strain, which could be defined as the influence region of the FPZ.
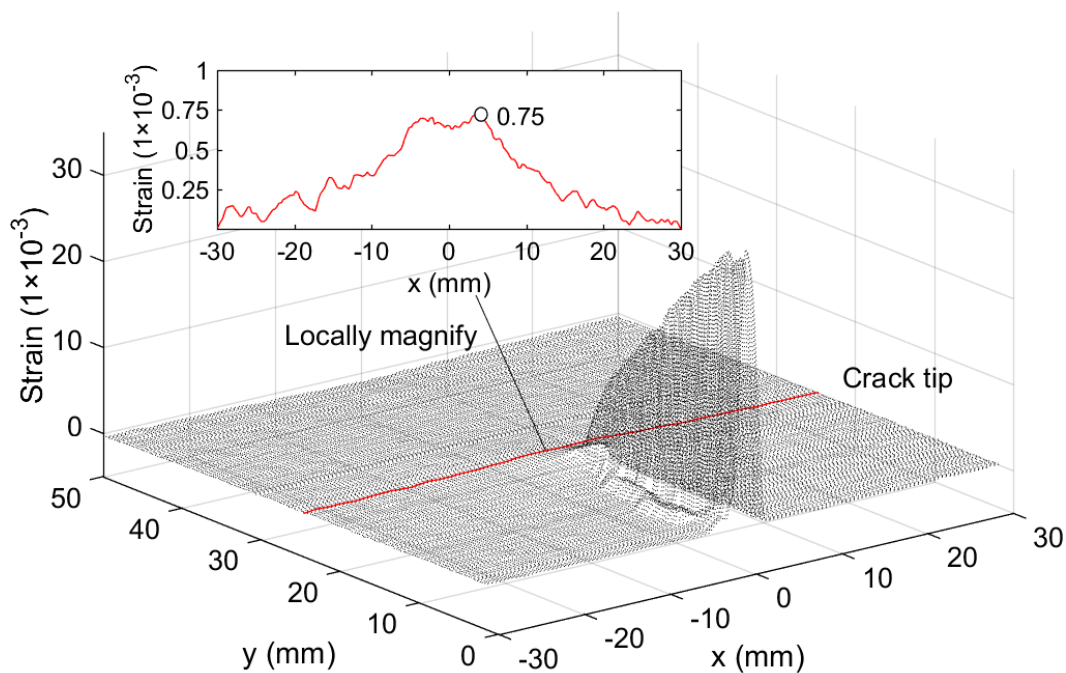

Fig. 5   3D profiles of strain filed in the x direction ε_{xx} at the peak load.

In this study, the FPZ was defined as the region where the strain ε_{xx} reached $0.75 \times$ 10^{-3}. The development of the FPZ were evaluated based on the in-plane strain contours of six typical loading stages (Fig. 4c), as shown in Fig. 6.
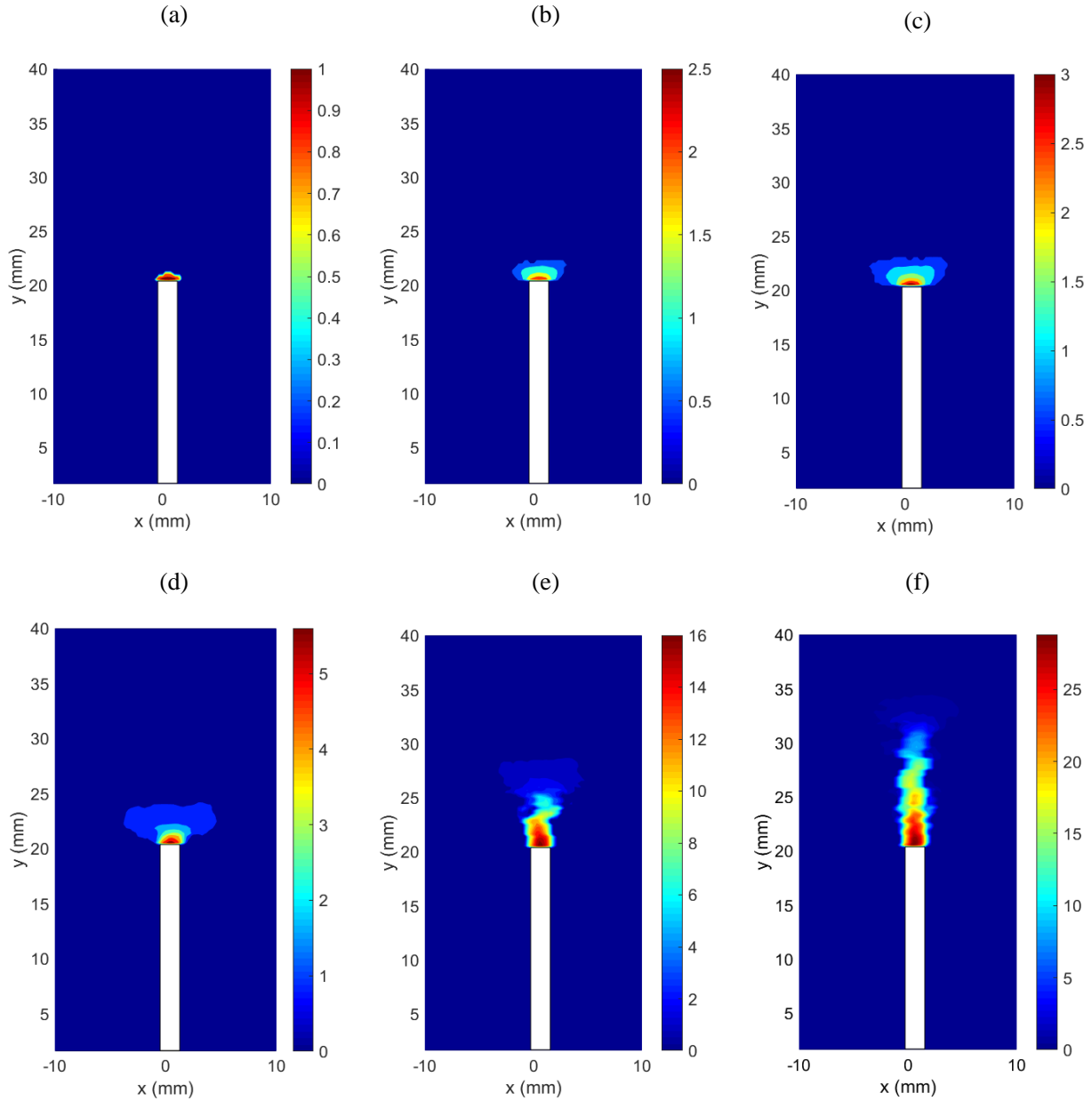

Fig. 6 Strain contours in the x direction of Sample 1 at different loading levels: (a) P_3 (pre-peak, 40% P_c), (b) P_5 (pre-peak, 74% P_c), (c) P_6 (pre-peak, 89% P_c), (d) P_7 (peak load, P_c), (e) P_8 (post-peak, 89% P_c), (f) P_9 (post-peak, 63% P_c) (unit: 1×10^{-3}).

At the pre-peak 40% of the peak load (P_3), the strain concentration occurred near the

initial notch tip and the material had some damage caused by the initiation of microcracks. It can be seen that a wide (horizontal) and thin (vertical) zone appears before the initiation fracture load (P_5, 74% of P_c in the pre-peak stage). Similar phenomenon in concrete was observed by Xu et al. [29] who indicated that this could not be considered as a substantial crack initiation because the surface of a beam was easier to fracture than the internal material. When the load reached P_5, a stable crack initialed from the notch tip and the FPZ formed an elliptical shape, which could be attributed to microcracks localization and extension [31]. After that, the FPZ developed relatively slowly before reaching the peak load (Fig. 6c).

At the peak load (P_6), the wake of the FPZ represented a band shape and its dimensions (length $\times$ width) were approximately 4.5 mm $\times$ 8.4 mm. It is obviously larger than 1.8 mm $\times$ 2.2 mm of IG11 graphite [10], which were estimated from the interference phase maps that neglected the extent of microcracks. As a considerable amount of strain energy accumulated in the previous loading process was released quickly, the crack propagated rapidly and the band shape of the FPZ became narrower and longer after the peak load. The width of the FPZ reduced as the crack propagated further, indicating that some microcracks partially closed with the expansion of the main crack. When the load reduced to 63% P_c, the FPZ was fully developed and presented an elliptical shape at the front followed by a narrow and long band shape. Similar observation on the FPZ shape of NBG10 and Gilsocarbon graphites was reported by Becker et al. [4], who utilized the strain mappings measured by DIC technique to gain further insight into the FPZ and pointed out that the general direction of strain localizations caused by microcracking was

predominantly parallel with the extrusion direction.

4.3. Double-K fracture toughness and fracture energy

From the evolution of the crack, it can be found that the whole fracture process in graphite beam can be distinguished into three different states, i.e., crack initiation, stable crack propagation and unstable fracture. Similar phenomenon in concrete was observed by Xu et al. [29, 32], who proposed a double-*K* fracture model (DKFM) to predict the crack propagation of quasi-brittle materials.

According to the DKFM, the fracture process of quasi-brittle materials is divided into three states: crack initiation, stable crack propagation and unstable fracture. Accordingly, the DKFM consists of two fracture parameters: initiation fracture toughness K_{Ic}^{ini} and unstable fracture toughness K_{Ic}^{un}. The K_{Ic}^{ini} is the inherent toughness of a material that resists the propagation of a crack and can be determined with the following equation [29]:

$$K_{Ic}^{ini} = 1.5 \frac{P_{ini}S}{D^2 t} \sqrt{a_0} F(\alpha_0) \tag{5}$$

$$F(\alpha_0) = \frac{1.99 - \alpha_0(1-\alpha_0)(2.15 - 3.93\alpha_0 + 2.7\alpha_0^2)}{(1+2\alpha_0)(1-\alpha_0)^{3/2}} \tag{6}$$

where P_{ini} is the initial fracture load, S, D and t are the beam span, depth and thickness, respectively, a_0 is the initial notch depth and $\alpha_0 = a_0/D$.

Similarly, the K_{Ic}^{un}, denoting the resistance of members to external forces in critical instability state, can be calculated by substituting the critical crack length a_c and the maximum load P_c for a_0 and P_{ini} in above formulas. Based on linear asymptotic superposition assumption [32], the critical effective crack length a_c can be evaluated by inserting the measured P_c, CMOD$_c$ and E into the following formula [33]:

$$a_c = \frac{2D}{\pi} \arctan \sqrt{\frac{tE}{32.6P_c} \text{CMOD}_c - 0.1135} \qquad (7)$$

As an essential fracture parameters to describe the fracture behavior and characterize the tension softening relationship of quasi-materials [34], the total fracture energy G_F can be evaluated by the work-of-fracture method [35] and determined from the entire load-deflection curve as following [36]:

$$G_F^{P-\delta} = \frac{A_0}{(D-a_0)t} \qquad (8)$$

in which A_0 is the area under the P-δ curve. The fracture parameters of each sample are tabulated in Table 1. It can be seen that various fracture parameters of XFEM model with a_0/D=0.4 obtained from numerical simulation are in excellent agreement with the experiment results, which further validates the accuracy and reliability of the XFEM simulation.

Table 1   Experimental and XFEM simulation results

Sample No.	P_{ini} (kN)	P_c (kN)	δ_c (mm)	CMOD_c (mm)	CTOD_c (mm)	$G_F^{P-\delta}$ (N/m)	a_c (mm)	E (GPa)	K_{Ic}^{ini} (MPa.m$^{1/2}$)	K_{Ic}^{un} (MPa.m$^{1/2}$)
1	0.637	0.848	0.182	0.082	0.013	183.2	21.6	10.3	0.903	1.316
2	0.652	0.874	0.187	0.085	0.010	172.0	20.7	9.3	0.925	1.290
3	0.603	0.819	0.164	0.086	0.013	164.1	22.3	10.2	0.855	1.321
4	0.638	0.853	0.193	0.083	0.016	176.1	21.8	10.5	0.905	1.342
5	0.745	0.959	0.17	0.083	0.011	179.6	20.7	10.4	1.056	1.412
Mean	0.655	0.871	0.179	0.084	0.011	175.0	21.4	10.1	0.929	1.336
Std dev.	0.053	0.053	0.012	0.002	0.002	7.4	0.705	0.483	0.076	0.046
a_0/D=0.2	1.136	1.557	0.172	0.050	0.014	197.1	11.2	10.0	0.955	1.394
a_0/D=0.3	0.830	1.180	0.159	0.065	0.013	176.6	16.2	10.0	0.903	1.362
a_0/D=0.4	0.643	0.899	0.160	0.084	0.014	172.2	21.1	10.1	0.912	1.356
a_0/D=0.5	0.477	0.673	0.162	0.100	0.011	169.6	25.4	10.2	0.909	1.314
a_0/D=0.6	0.344	0.470	0.177	0.127	0.011	165.8	30.6	10.4	0.928	1.325

Notes: P_c, δ_c, CMOD_c, CTOD_c and a_c are the load, deflection, CMOD, CTOD and effective crack length at the peak, respectively. "$a_0/D=\alpha_0$" implies XFEM models with different initial crack-depth ratio α_0.

The $K_{\mathrm{I}c}^{ini}$ and $K_{\mathrm{I}c}^{un}$ of the graphite are approximately 0.855-1.056 MPa.m$^{1/2}$ and 1.29-1.412 MPa.m$^{1/2}$, respectively. The measured values of $K_{\mathrm{I}c}^{ini}$ for the NG-CT-01 graphite are similar with the initial value (about 0.8 MPa.m$^{1/2}$) of K_{R} resistance curves for PGA graphite obtained by Ouagne et al. [37], who employed a video camera to determine the crack growth length in compact tension specimens. The $K_{\mathrm{I}c}^{ini}$ values are larger than that of concrete (about 0.2-0.5 MPa.m$^{1/2}$) obtained by Ince et al. [38] using split-tension specimens. This can be explained as the tensile strength of graphite (about 24 MPa) is higher than that of concrete (about 2.8-3.4 MPa), thus it contributes to more inherent toughness of the material. The values of $K_{\mathrm{I}c}^{un}$ for NG-CT-01 graphite are close to the fracture toughness of 1.30 ± 0.1 MPa.m$^{1/2}$ of Gilsocarbon graphite determined by Becker et al. [4], the values of 1.10 ± 0.07 MPa.m$^{1/2}$ and 1.15 ± 0.02 MPa.m$^{1/2}$ for the NBG-18 graphite (South Africa) and the PCEA grades (USA), respectively, obtained by Chi [9].

4.4. COD profiles

The COD profiles reflecting both the crack opening and crack growth are necessary to quantitatively analyze crack propagation of nuclear graphite and employ the IDCM to determine the TSC. In the experimental measurement, the COD profiles can be determined from the relative horizontal displacements along the two adjacent faces of the crack after eliminating the elastic deformation in the crack opening [12]. In the XFEM analysis, the COD is directly calculated from the relative horizontal displacements along two cross sections beside the main crack and elastic deformation around the FPZ can be neglected due to ideal boundary conditions in numerical simulation.

Fig. 7 shows the COD profiles obtained by ESPI measurement and XFEM simulation

under three typical loading steps (see Fig. 4c). The coordinate y corresponds to the position in the vertical direction (see Fig. 2b) which is zero at the mouth of the center notch. From the COD profiles, the crack tip is identified as the position at which the COD reduces to zero and the length of crack is defined as the distance between the notch mouth and crack tip. At the loading point P_3 (40% P_c in pre-peak loading stage), the COD at the notch tip (y = 20 mm), termed as the CTOD, is about 3 μm and the crack length is about 23 mm. At the peak load P_7, the CTOD is about 13 μm with a crack length of about 25 mm. At the loading point P_9 (63% P_c in the post-peak loading stage), the CTOD and the crack length are about 58 μm and 35 mm, respectively.
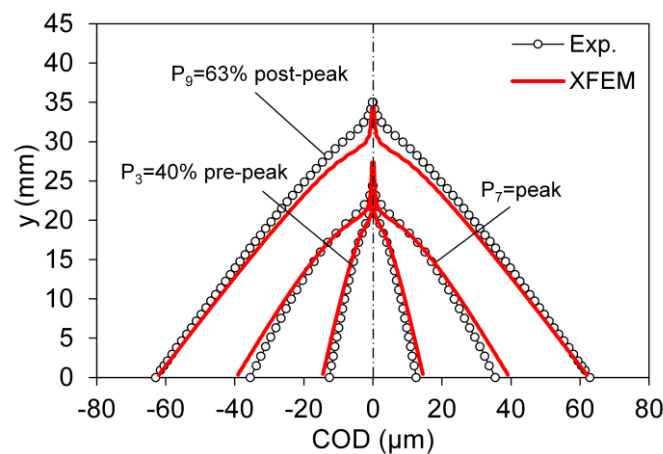
Fig. 7   COD profiles of Sample 1 at different loading levels.

Comparing with the experimental results, the COD profiles obtained by the XFEM at the same loading levels are quite similar during the whole loading process, especially in the pre-peak loading stage. After the peak load, although the position of the crack tip and the CMOD obtained by the XFEM and ESPI are almost identical, the numerical COD near the crack tip is smaller than the experimental result. This is because slow development of the FPZ in the pre-peak loading stage had little influence on the crack opening, while rapid growth of the FPZ in the post-peak loading stage had a considerable influence on crack

opening. Therefore, the characteristics of the FPZ are critical to simulate the crack propagation path by FE method [6, 18].

4.5. Tension softening curve

In the IDCM, three point bending beam was simulated by using a FE program written in FORTRAN code which is based on linear elastic fracture mechanics except a cohesive crack is integrated into the FPZ to create nonlinear fracture resistance. The cohesive stress distribution along the cohesive crack is computed based on measured displacement and adjusted through a displacement collocation process. Due to the symmetry of the specimen, only a half of the beam was analyzed, as shown in Fig. 8. A total of 450 9-node hybrid elements [39] were used in this study. The bulk material was considered to behave in a linear-elastic manner. The Poisson's ratio was assumed to be 0.2 in the analysis as it had little influence on the fracture behavior of nuclear graphite [31].
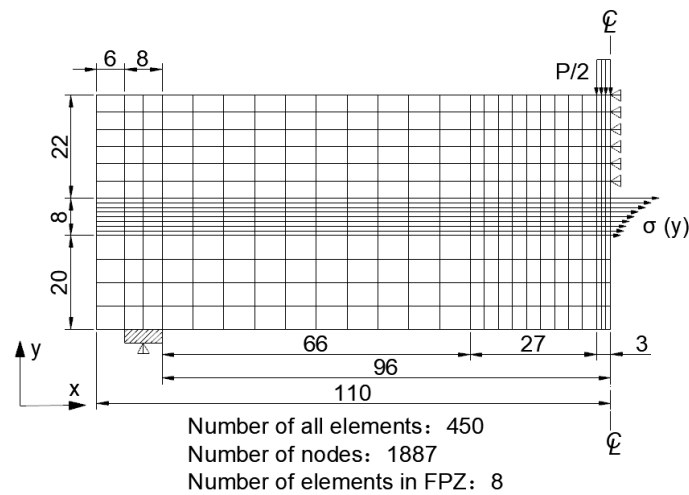
Fig. 8   Specimen configuration and FE meshes (unit: mm).

Taking Sample 1 at the post-peak loading level of 89% P_c (P_8) as an example, numerical model was built based on the concept of cohesive crack model (CCM) [15] and the COD profiles obtained by XFEM simulation. The notch section was divided into three

zones (see Fig. 8) in the y direction : the real crack zone corresponding to the initial notch part (y = 0-20 mm), the cohesive crack zone depends on the length of the FPZ (y = 20-28 mm) and the linear-elastic zone in which crack opening is 0 (y = 28-50 mm). In the linear elastic zone, only vertical displacement was allowed by imposing horizontal constraints on the nodes. In the cohesive crack zone, the cohesive stress $\sigma(y)$ was calculated by the simulated COD profiles and applied to the nodes to simulate the fracture resistance of the FPZ. By minimizing the discrepancy between the calculated and simulated displacements at each analysis steps, the cohesive stress was determined in a step by step manner to form a complete TSC.

By utilizing the combined XFEM-IDCM, the TSC of NG-CT-01 graphite is determined and shown in Fig. 9. The result of present study was compared with the results obtained by Su et al. [5], who using the IDCM to evaluate the TSCs, and good consistence can be observed. Fig. 10 compares the computed load-displacement curves with the measured results. There are two types of computed results: the calibrated displacements before the complete TSC is established, marked as the solid circles, and the predicted displacements for verifying the established TSC after the FPZ is fully developed, marked as the hollow circles in Fig. 10. Excellent agreement can be found during the entire loading process, validating the feasibility and accuracy of the proposed method.
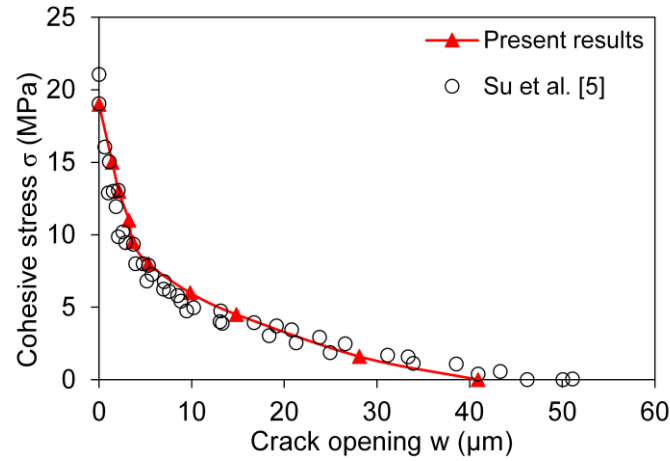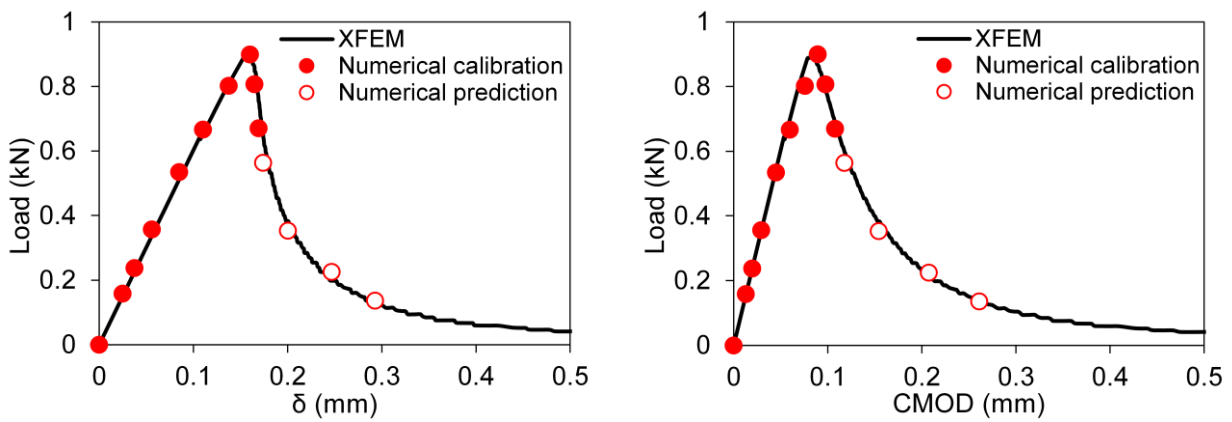
Fig. 9   The TSC of NG-CT-01 graphite.

Fig. 10   Numerical and XFEM simulated load-displacement curves: (a) *P-δ* curves, (b) *P*-CMOD curves.

5. The influence of initial crack to depth ratio

In the XFEM, the crack geometry is completely independent of the FE mesh and remeshing is not required [20, 21]. Therefore, the same mesh model can be employed to simulate the crack propagation with different initial crack lengths.

Keeping the material parameters and grid partition of the XFEM model unchanged, the initial crack lengths a_0 were set to 10 mm,15 mm, 20 mm, 25 mm and 30 mm and the corresponding initial crack length to beam depth ratios a_0/D were 0.2, 0.3, 0.4, 0.5 and 0.6, respectively.

5.1. Variation of load-displacement curves

The P-CMOD and P-CTOD curves of various numerical models with different initial crack lengths are shown in Fig. 11. From Fig. 11 and Table 1, it can be observed that, with the increase of initial crack length, both the slope of the linear segment of the curve, the initiation fracture load and the maximum load decrease as the ligament of the beam at the mid-span section reduces. At the peak load, the values of $CMOD_c$ increase while the values of $CTOD_c$ almost keep unchanged with the increase of a_0/D.
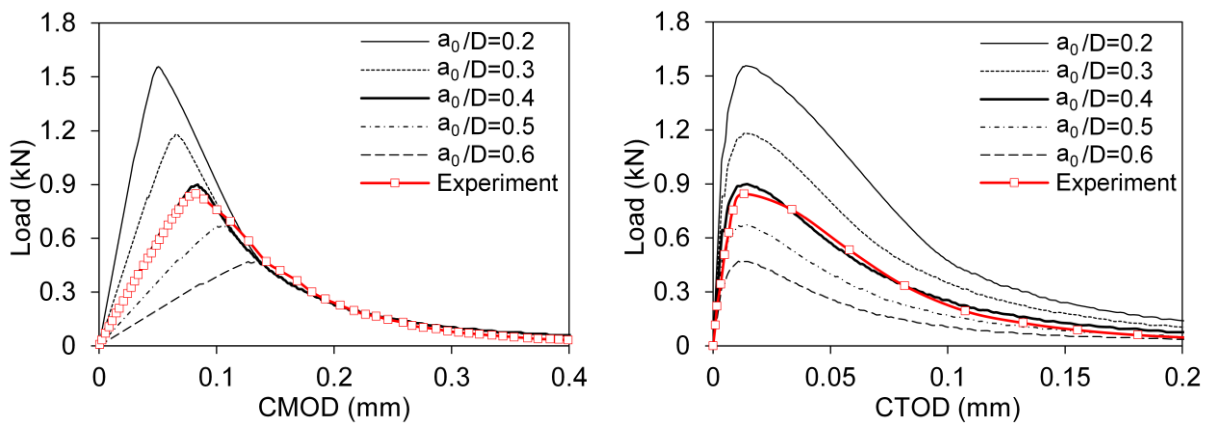

Fig. 11   Variations of load-displacement curves with different a_0/D: (a) load-CMOD curves, (b) load-CTOD curves.

5.2. Variation of double-K fracture parameters

The variations of the load, CMOD, fracture toughness and CTOD of graphite beams with different a_0/D are presented in Fig. 12. It can be seen from Fig. 12a that the initiation fracture and maximum load decrease with the increasing a_0/D, while the ratio of P_{ini}/P_c keeps a stable level of about 0.72. As shown in Fig. 12b, the CMOD at the initiation fracture load (denoted as $CMOD_{ini}$) and at the peak load (denoted as $CMOD_c$) increased with the increase of a_0/D. The increase extent of $CMOD_c$ was larger than that of $CMOD_{ini}$, which can be explained as the initial fracture load depends on the material inherent toughness while the maximum load is related to the fracture ligament of the beam.
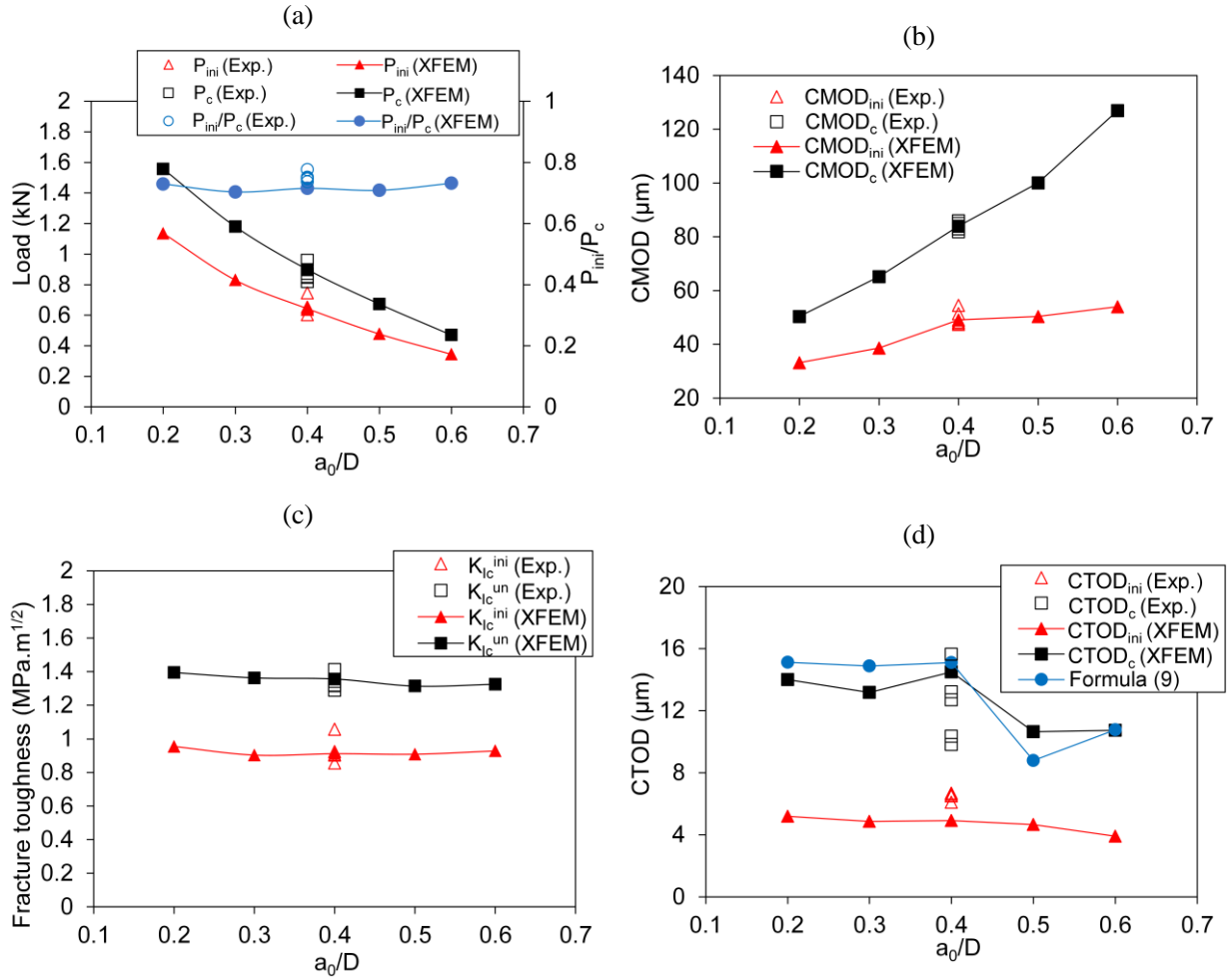
Fig. 12   Variations of fracture parameters at initial and unstable fracture load with different a_0/D: (a) load, (b) CMOD, (c) fracture toughness, (d) CTOD.

Although the numerical results at the initial and unstable fracture points have been some variations with different a_0/D, the initiation fracture toughness and unstable fracture toughness are independent of the a_0/D, as shown in Fig. 12c. The K_{Ic}^{ini} and K_{Ic}^{un} of various a_0/D remains about 0.92 MPa.m$^{1/2}$ and 1.35 MPa.m$^{1/2}$, respectively. The specific values of double-K fracture parameters with different a_0/D are listed in Table 1.

Considered as an essential fracture parameter in two parameters fracture model [40], the CTOD$_c$ is usually calculated by the relationship of CMOD and CTOD due to the inconvenience of experimental measurement. Based on the LEFM, the CTOD$_c$ can be determined by the following formula [41]:

$$\mathrm{CTOD_c}=\mathrm{CMOD_c}\times\left\{\left(1-\frac{a_0}{a_c}\right)^2+\left(1.081-1.149\frac{a_c}{D}\right)\left[\frac{a_0}{a_c}-\left(\frac{a_0}{a_c}\right)^2\right]\right\}^{1/2} \qquad (9)$$

From Fig. 12d, it can be found that the calculated results of $\mathrm{CTOD_c}$ agree well with the XFEM results and the ESPI results. With the increase of a_0/D, the CTOD at the initial fracture load, denoted as $\mathrm{CTOD_{ini}}$, remains around 4.7 μm and the values of $\mathrm{CTOD_c}$ are about 12.3 ± 2.2 μm.

5.3. Variation of tension softening curves

Using the combined XFEM-IDCM proposed in this study, the TSCs of graphite beams with various a_0/D are determined. The displacements, including the δ and CMOD, calculated by the FE analysis using FORTRAN code are compared to the XFEM simulated displacements in Fig. 13 and excellent agreement has been observed, which further verifies the accuracy of the TSCs evaluated by the proposed method.
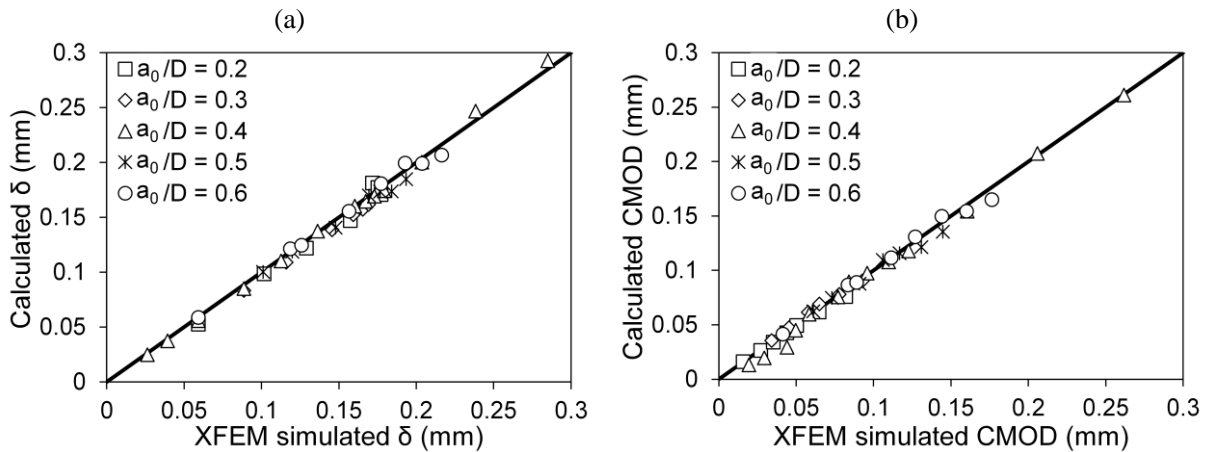

Fig. 13   Comparisons of XFEM simulated and FE calculated displacement: (a) deflection δ, (b) CMOD.

The TSCs of graphite beams with different a_0/D are presented in Fig. 14. From the figure, it can be observed that the TSCs are independent on the a_0/D ratio, which confirms that the TSC can be considered as a material property and characterized by the tensile

strength f_t and the cohesive fracture energy G_F [42]. The cohesive fracture energy G_F is the external energy absorbed by a unit fracture area and can be derived from the area under a fully-developed TSC as follows:

$$G_F^{TSC} = \int_0^{w_c} \sigma(w)\mathrm{d}w \tag{10}$$

where w_c is the critical crack opening at which the cohesive stress becomes zero. The specific parameters that are employed to describe the TSCs are tabulated in Table 2. From the table, it can be seen that the mean value of the fracture energy determined by the TSC is 173.8 N/m, which is quite close to that of 175 N/m calculated from the P-δ curve. The difference of the fracture energy obtained by the two methods is attributed to the fact that externally applied energy to the beam was dissipated partly due to other process, such as friction, rather than fully due to the crack formation [43].
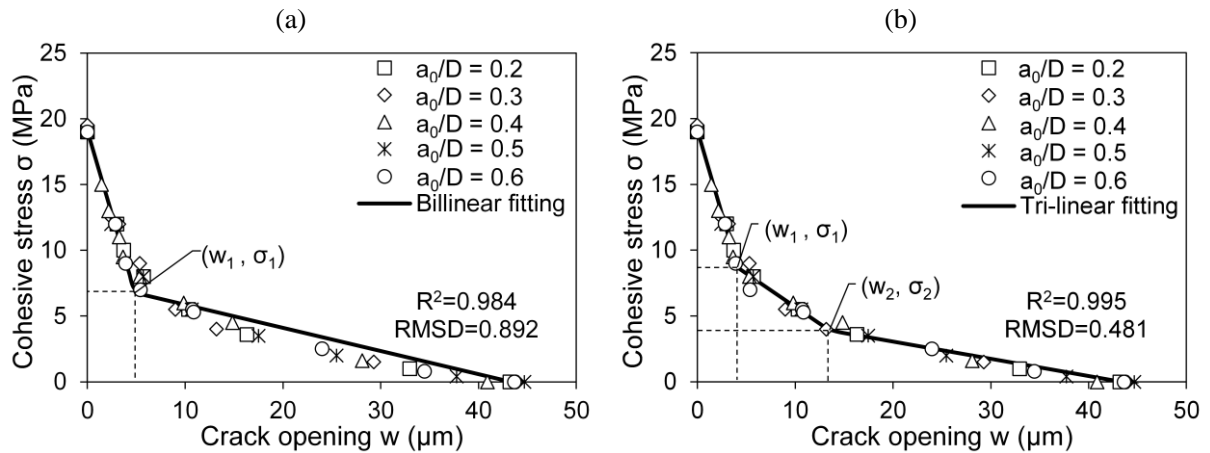

Fig. 14   Approximations of the estimated TSCs with (a) bilinear fitting, (b) tri-linear fitting.

Table 2   Fracture parameters estimated from the proposed method

a_0/D	f_t (MPa)	w_c (µm)	G_F^{TSC} (N/m)	Bilinear fitting		Tri-linear fitting		
				σ_1 (MPa)	w_1 (µm)	σ_1 (MPa)	w_1 (µm)	σ_2 (MPa)	w_2 (µm)
0.2	19	43.2	174.1						
0.3	19.5	43.8	174.4	6.769	4.862	8.673	4.111	3.901	13.506
0.4	19	40.9	174.8						
0.5	19	44.7	172.6						

0.6	19	43.6	173.3
Mean	19.1	43.3	173.8
Std dev.	0.224	1.42	0.885

Using regression analysis, the TSCs obtained in the present study were approximated to the bilinear [44] and tri-linear [45] curves and the approximation results are shown in Fig. 14. The stress and crack opening at the kink points for defining the bilinear and tri-linear curves are listed in Table 2. From the Fig. 14, it can be seen that better approximation is provided by tri-linear fitting at the tail of the TSCs. The effect of approximation can be judged by the degree of fit (R^2, the closer to 1, the better the fitting is) and the root-mean-square deviation (RMSD, the closer to 0, the smaller the deviation between fitting and original results.). R^2 and RMSD are 0.984 and 0.892 respectively for bilinear fitting, and are 0.995 and 0.481 respectively for tri-linear fitting. Therefore, the tri-linear curve is more suitable for approximating the TSC of nuclear graphite, which can provide an evidence for the next discussion about the correlation between the softening behavior and fracture mechanism of the FPZ.

5.4. Variation of the FPZ length

The length of the FPZ, l_{FPZ}, can be evaluated based on the CCM and the computational procedure has been detailed by Chen et al. [10]. The characteristic crack opening width w_c is taken as 43.3 μm in this study (Table 2). To investigate the variation of the FPZ length during the whole fracture process, the l_{FPZ} was plotted against $(a-a_0)/(D-a_0)$ (the ratio of crack extension length to the ligament length) and depicted in Fig. 15. As shown in Fig. 15, the length of the FPZ increased steadily in the pre-peak stage and $(a-a_0)/(D-a_0)$ is about 0.2 at the peak load. After the peak load, the FPZ length increased rapidly and reached the maximum value when the FPZ was fully developed and

$(a-a_0)/(D-a_0)$ is approximately 0.35-0.45. After that, the length of the FPZ decreased gradually as the crack further extended. Similar development trends of the FPZ in concrete was observed by Wu et al. [18] and they found that the FPZ length increased during crack propagation but decreased after the FPZ was fully developed when $(a-a_0)/(D-a_0)$ was about 0.91. The ratio in graphite material is much lower, which indicates that the size of a fully-developed FPZ in graphite is much smaller, thus its fracture behavior presents more brittleness than other quasi-brittle materials like concrete.
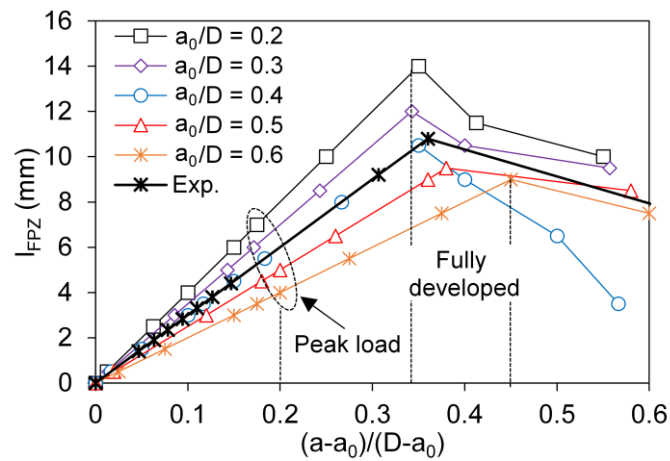

Fig. 15   Variations of the FPZ length with $(a-a_0)/(D-a_0)$.

The FPZ length at the peak load and at which the FPZ is fully developed are presented in Fig. 16. It can be found that, with the increase of initial crack length, the length of ligament decreased accordingly, thus the development of the FPZ was constrained by the upper boundary, causing both the FPZ length at the peak load and the fully developed FPZ length decreased with the a_0/D increased. Similar experimental observation in concrete was reported by Wu et al. [18].
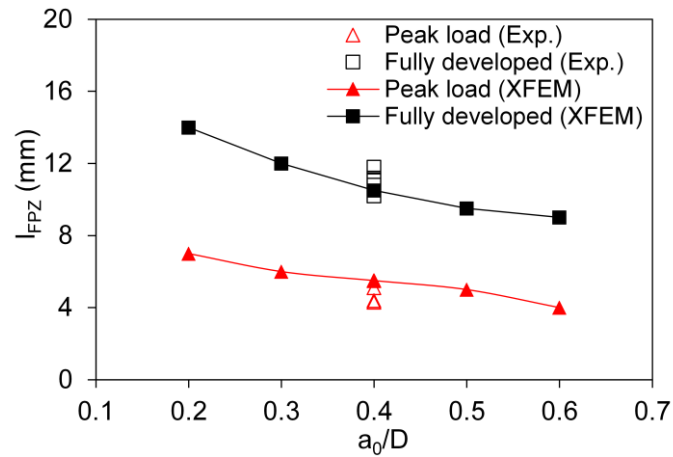
6. Discussions

6.1 Correlation of the FPZ and tension softening behavior

Although graphite shows more brittleness than other quasi-brittle materials, the fracture behavior of graphite still exhibits non-linear and quasi-brittle due to the existence of the FPZ near the crack tip. It is of great significance to evaluate the relationship of the physical mechanism in FPZ and tension softening behavior to further clarify the non-linear fracture behavior of graphite.

The correlation between the softening behavior and fracture mechanism of the FPZ in concrete has been previously investigated by Nomura et al. [46], who pointed out that the beginning of descending branch and tail of the TSC corresponded to the microcracking process and the bridging effect respectively. In order to study the correlation between the TSC and the FPZ mechanism in graphite, a profile of the fully developed FPZ (Fig. 6f) and the cohesive stress distribution calculated by the experimental COD (Fig. 7) and the estimated TSC (Fig. 9) are presented in Fig. 17. It can be observed that, the local strain is relatively small and distributed widely near the tip, indicating a slight damage to the material. Thus the FPZ emerged an elliptical shape at the front ($y \approx 32\text{-}34.5$ mm), which is

followed by a high strain concentration and the shape of the FPZ shows a narrow and long

band ($y \approx$ 23.5-29.4 mm). There is also a transition zone ($y \approx$ 29.4-32 mm) between the

elliptical and the band regions, which contains the geometric characteristics of the two

regions. It can also be seen that the cohesive stress distribution can be divided into three

segments, which is consistent with the previous finding that the tri-linear curves can

provide the best approximation for the estimated TSCs. These three segments are just

corresponding to the observed three sections of the FPZ, as shown in Fig. 17.
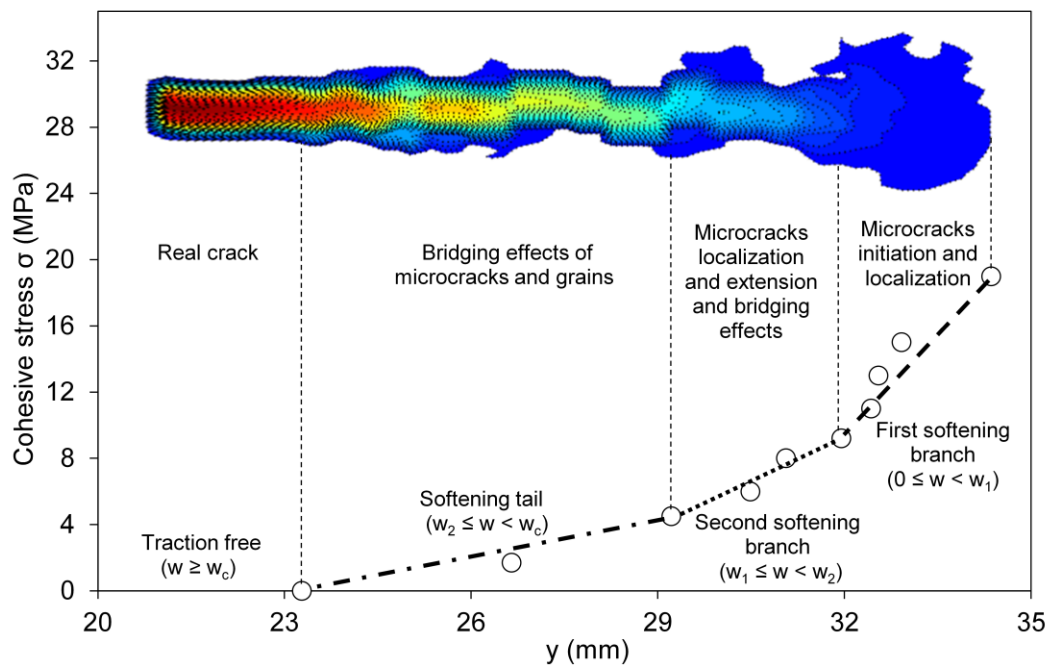

Fig. 17   Correlation of tension softening behavior and mechanism in FPZ.

Combining the general interpretation of the tension softening relationship in terms of

mechanisms in the FPZ proposed by Nomura et al. [46] and the observed results in the

present study, the softening behavior in the FPZ of graphite can be characterized by a

tri-linear model, as shown in Fig. 17. The first softening branch ($0 \leq w < w_1$, marked as

dash line in Fig. 17) is considered to be influenced by microcracks initiation and

localization, which corresponds the damage zone ahead of the stable crack and occurs

before the initial fracture load (see Fig. 6a). The second softening branch ($w_1 \leq w < w_2$, marked as dotted line in Fig. 17) represents a fracture process when the microcracks are localized and extended and the bridging effect occurs, which enters stable crack propagation stage (see Fig. 6c). The softening tail ($w_2 \leq w < w_c$, marked as dash-dotted line in Fig. 17) is attributed to the bridging mechanism of microcracks and grains under low transmitted stress, causing the crack extends rapidly (see Fig. 6e) and it shows a narrow and long band shape in the wake. When $w \geq w_c$, the real crack has been formed as there is no residual stress and the traction is free.

As shown in Fig. 18, the fully developed FPZ of graphite represents an elliptical shape near the tip followed by a narrow and long band, while the FPZ in concrete material shows an irregular band as reported by Otsuka et al. [47] and Wu et al. [18], who utilized the X-ray technique and DIC technique to observe the cracking zone, respectively. The reason for this difference of two materials is perhaps due to the smaller grain size of graphite than that of concrete. As presented in Fig. 18, the microcracks initiated and propagated along the weaker particle-matrix in aggregate-containing porous materials [3]. For graphite, the small grain (about 25 μm) brings about a relatively narrow range of the bridging zone than the microcracking zone, which results in the FPZ shape of graphite shows an elliptical shape around the front and a narrow and long band in the wake. While for concrete, the maximum aggregate is about 8 mm [18], which is close to or even greater than the width of the microcracking zone, causing the appearance of a relatively wide band along the whole length of the FPZ.
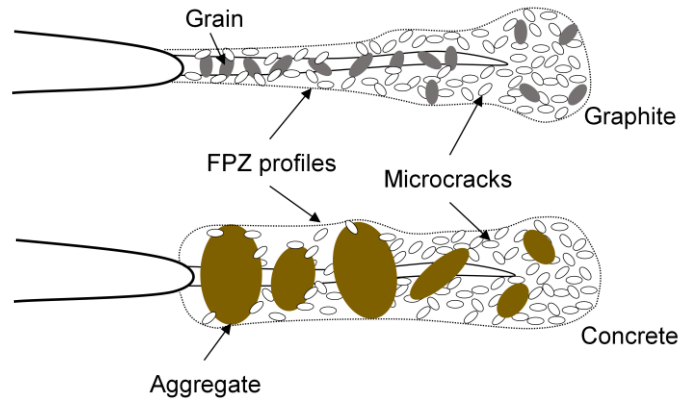
Fig. 18   Schematic illustration of the FPZ profiles in graphite and concrete.

It was worth mentioning that, when the size of the specimen is large enough, the length of FPZ is actually relatively small compared with the total length of the crack, thus the nonlinear behavior can be ignored and the LEFM becomes applicable [12]. Since the ligament of the beam in this study is 30 mm, it can be deferred that non-linear behavior cannot be neglected for any length scale smaller than that.

Generally, the XFEM simulation using linear softening constitutive relation can provide satisfactory agreement between experimental and numerical results. However, linear softening constitutive model is insufficient to characterize the relationship of the softening behavior and fracture mechanism of the FPZ while the tri-linear softening curve can. In addition, due to the difficulty of measuring crack opening displacement (COD) experimentally, XFEM simulation in this study only provides an alternative to obtain the COD information which is required to be input in the FE model using the IDCM.

6.2 Correlation of the FPZ and crack growth resistance curve

To evaluate the effect of the FPZ during the complete crack propagation in graphite, crack growth resistance curve [7, 48] in the form of mode I fracture toughness (K_I), calculated by putting the applied load and the measured crack length by ESPI into the Eqs

(5) and (6), versus the crack extension length ($\Delta a = a - a_0$) is shown in Fig. 19. From Table 2 and Fig. 12d, it can be found that the values of the CTOD at the initiation fracture load and peak load were about 4.7 ± 0.8 μm and 12.3 ± 2.2 μm, respectively, which corresponds to the crack opening w_1 (4.1 μm) and w_2 (13.5 μm) of two kink points in tri-linear fitting in Fig. 19. This helps to interpret the K_I-curve behavior using the TSC and further verifies that the double-K fracture criterion can be applied to predict crack propagation over the fracture process in graphite.
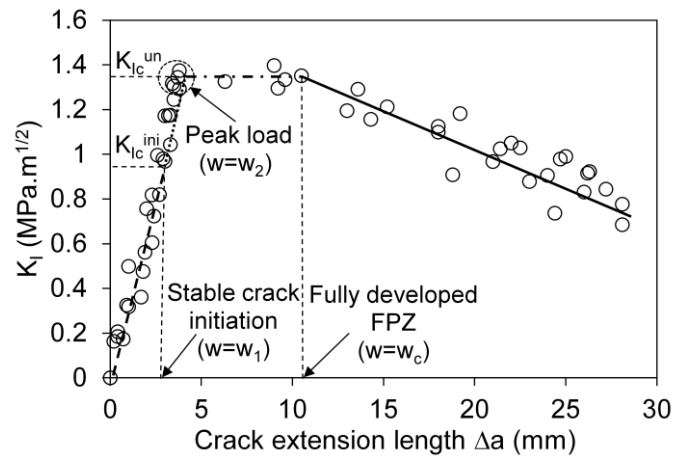

Fig. 19   Fracture toughness versus crack extension length.

As shown in Fig. 19, the shape of the K_I curve is similar to the experimental results reported by other researchers [7, 17, 37, 49]. It can be observed that, when $K_I < K_{Ic}^{ini}$, the crack opening w is smaller than w_1 in the tri-linear fitting. The corresponding fracture toughening mechanism in the FPZ is microcracking which causes the energy dissipation and the increase of the resistance in crack growth. After the crack initiation ($K_I = K_{Ic}^{ini}$), the crack develops steadily and the increase in crack growth resistance are attributed to the development of crack bridging zone by graphite filler grains and microcracks [37, 48, 49], which corresponds to the second softening branch of the tri-linear model (see Fig. 17). After the peak load ($K_I = K_{Ic}^{un}$), there is a short plateau region where the crack extension

length is between 4-10.5 mm. Similar phenomenon was observed in polycrystalline graphite by Ouagne et al. [37], who pointed out that the frontal zone and wake zone might have reached steady state values at this stage. It can be seen from Fig. 6d-f that the frontal microcracking zone remains relatively stable while the wake bridging zone develops quickly. The plateau region of K_I-curve is corresponding to the softening tail of the TSC (see Fig. 17), at which the crack opening increases while transmits a low transmitted stress. With low cohesive stress, the traction force that prevents the propagation of cracks is small, causing the crack propagates unstably while the crack growth resistance remains a stable level.

When the crack extends to approximately 10.5 mm, which is close to the fully developed FPZ length (see Fig. 15), the K_I decreases slightly with the crack propagates. It may be due to the fact that the FPZ length decreases with the further expansion of the crack after the FPZ is fully developed as shown in Fig. 15. The decreasing trend of crack growth resistance curve was also observed by Sakai et al. [49], which was attributed to edge effect produced by the geometrical interaction of the large-scale microcracking zone with the end surface of the specimen. Therefore, it can be concluded that the reduced FPZ length after the FPZ is fully developed is due to the boundary effect.

7. Conclusions

In this study, fracturing behaviors of NG-CT-01 graphite subjected to three-point bending were investigated and following conclusions can be drawn:

(1) The extent of the FPZ is defined as the damage zone where the tensile strain ε_{xx} is more than 0.75×10^{-3}. Based on the in-plane strain contours obtained by ESPI

measurement, crack propagation in graphite can be divided into three stages: crack initiation, stable crack propagation and unstable fracture. A fully developed FPZ is of an elliptical shape followed by a narrow and long band.

(2) A numerical analysis is conducted using ABAQUS coupled with XFEM to simulate the fracture behavior of graphite beam. The XFEM simulation results are compared with the experimental results and excellent agreement is observed, demonstrating the feasibility and accuracy of the numerical model. By combining the XFEM and IDCM, the TSC of NG-CT-01 graphite is determined.

(3) Fracture responses of graphite beam with $a_0/D = 0.2\text{-}0.6$ are investigated by using XFEM simulation. As the increase of a_0/D, the $CMOD_{ini}$ and $CMOD_c$ increases while the P_{ini} and P_c decreases. The K_{Ic}^{ini} and K_{Ic}^{un} are independent on the initial crack length and keep stable values of about 0.921 and 1.351 MPa.m$^{1/2}$, respectively. The $CTOD_{ini}$ and $CTOD_c$ nearly remain unchanged with different a_0/D. The FPZ length increases first as crack propagation, then decreases due to the edge effect after the FPZ is fully developed when the crack extension length to ligament length ratio is about 0.35-0.45.

(4) The relationship of the tension softening behavior and fracture mechanism in the FPZ is evaluated by a tri-linear model. The first descending branch in TSC corresponds to the microcracks initiation and localization, causing the elliptical shape near the FPZ tip, and the tail of the TSC is mainly attributed to the bridging effect, resulting in the narrow and long band in the FPZ wake. There exists a transition region between them, which contains both microcracking and bridging effect.

(5) Double-K fracture criterion is employed to describe crack propagation during the

fracture process in graphite. The crack propagates stably firstly after the crack initiates (K_{I} = K_{Ic}^{ini}) and the crack growth resistance increases due to the distributed microcracks and bridging mechanism. After the load reaches its peak (K_{I} = K_{Ic}^{un}), the crack propagates unstably and there is a short plateau region in K_{I}-curve due to the low transmitted stress. The followed descending part of K_{I}-curve is attributed to the decreased FPZ length after the FPZ is fully developed, caused by the boundary effect.

Acknowledgement

References

[1] T.D. Burchell, A microstructurally based fracture model for polygranular graphites, Carbon 34(3) (1996) 297-316.

[2] T.D. Burchell, L.L. Snead, The effect of neutron irradiation damage on the properties of grade NBG-10 graphite, J Nucl Mater 371(1-3) (2007) 18-27.

[3] P.J. Heard, M.R. Wootton, R. Moskovic, P.E.J. Flewitt, Crack initiation and propagation in pile grade A (PGA) reactor core graphite under a range of loading conditions, J Nucl Mater 401(1) (2010) 71-77.

[4] T.H. Becker, T.J. Marrow, R.B. Tait, Damage, crack growth and fracture characteristics of nuclear grade graphite using the Double Torsion technique, J Nucl Mater 414(1) (2011) 32-43.

[5] R.K.L. Su, H.H. Chen, S.L. Fok, H. Li, G. Singh, L. Sun, L. Shi, Determination of the tension softening curve of nuclear graphites using the incremental displacement collocation method, Carbon 57 (2013) 65-78.

[6] M. Mostafavi, S.A. McDonald, P.M. Mummery, T.J. Marrow, Observation and quantification of three-dimensional crack propagation in poly-granular graphite, Eng Fract Mech 110 (2013) 410-420.

[7] H. Li, J. Li, G. Singh, A. Fok, Fracture behavior of nuclear graphite NBG-18, Carbon 60 (2013) 46-56.

[8] T.D. Burchell, D. Erdman, The shear fracture toughness, KIIc, of graphite, Carbon 98 (2016) 267-279.

[9] S.-H. Chi, Comparison of fracture toughness (K IC) and strain energy release rate (G) of selected nuclear graphites, J Nucl Mater 476 (2016) 188-197.

[10] H.H.N. Chen, R.K.L. Su, S.L. Fok, H.G. Zhang, Fracture behavior of nuclear graphite under three-point bending tests, Eng Fract Mech 186 (2017) 143-157.

[11] S.M. Barhli, L. Saucedo-Mora, M.S.L. Jordan, A.F. Cinar, C. Reinhard, M. Mostafavi, T.J. Marrow, Synchrotron X-ray characterization of crack strain fields in polygranular graphite, Carbon 124 (2017) 357-371.

[12] Y.X. Tang, H.N. Chen, Characterization on crack propagation of nuclear graphite under three-point bending, Nuclear Materials and Energy 20 (2019) 100687.

[13] A. Hodgkins, T.J. Marrow, M.R. Wootton, R. Moskovic, P.E.J. Flewitt, Fracture behaviour of radiolytically oxidised reactor core graphites: a view, Mater Sci Tech-Lond 26(8) (2010) 899-907.

[14] H.H. Chen, R.K.L. Su, Tension softening curves of plain concrete, Constr. Build. Mater. 44 (2013) 440-451.

[15] A. Hillerborg, M. Modéer, P.E. Petersson, Analysis of crack formation and crack growth in concrete by means of fracture mechanics and finite elements Cement Concrete Res 6(6) (1976) 773-781

[16] R.K.L. Su, H.H.N. Chen, A.K.H. Kwan, Incremental displacement collocation method for the evaluation of tension softening curve of mortar, Eng Fract Mech 88 (2012) 49-62.

[17] A. Hodgkins, T.J. Marrow, P. Mummery, B. Marsden, A. Fok, X-ray tomography observation of crack propagation in nuclear graphite, Mater Sci Tech-Lond 22(9) (2006) 1045-1051.

[18] Z.M. Wu, H. Rong, J.J. Zheng, F. Xu, W. Dong, An experimental investigation on the FPZ properties in concrete using digital image correlation technique, Eng Fract Mech 78 (2011) 2978–2990.

[19] J. Marrow, D. Liu, S.M. Barhli, M. Saucedo, D.M. Collins, Vertyagina, Yelana, P.E.J. Flewitt, D. Smith, In situ measurement of the strains within a mechanically loaded polygranular graphite, Carbon 96 (2016) 285-302.

[20] T. Belytschko, T. Black, Elastic crack growth in finite elements with minimal remeshing, Int J Numer Meth Eng 45(5) (1999) 601-620.

[21] N. Moës, J. Dolbow, T. Belytschko, A finite element method for crack growth without remeshing, Int J Numer Meth Eng 46(1) (1999) 131-150.

[22] Y.X. Tang, H.N. Chen, Simulation of crack propagation in concrete based on extended finite element method, Key Engineering Materials 783 (2018) 165-169.

[23] H.D. Huynh, P. Tran, X. Zhuang, H. Nguyen-Xuan, An extended polygonal finite element method for large deformation fracture analysis, Eng Fract Mech 209 (2019) 344-368.

[24] RILEM, TC 89-FMT Fracture Mechanics of Concrete, Determination of fracture parameters (KIcs and CTODc) of plain concrete using three-point bend tests, Mater Struct 23(6) (1990) 457-460.

[25] Dantec-Ettemeyer, ISTRA for Windows, Version 3.3.12, (2001).

[26] H.H. Chen, R.K.L. Su, A.K.H. Kwan, A.S.L. Fok, Correction of strain errors induced by small rigid-body motions in electronic speckle pattern interferometry measurement, HKIE Transactions 20 (2013) 1-11.

[27] S.P. Shah, Determination of fracture parameters (KIcs and CTODc) of plain concrete using three-point bend tests, Mater Struct 23(6) (1990) 457-460.

[28] H.H. Chen, R.K.L. Su, Experimental study on fracture behavior of pre-notched mortar beams using ESPI technique, Recent Researches in Hydrology, Geology and Continuum Mechanics (2011) 32-37.

[29] S.L. Xu, H.W. Reinhardt, Determination of double-K criterion for crack propagation in quasi-brittle fracture, Part I: Experimental investigation of crack propagation, Int J Fracture 98(2) (1999) 111-149.

[30] S.L. Xu, X.F. Zhang, B.U. Dan, Relationship between crack tip opening displacement (CTOD) and crack mouth opening displacement (CMOD) throughtout development of concrete crack (in Chinese), Engineering Mechanics 28(5) (2011) 64-70.

[31] S. Fazluddin, Crack growth resistance in nuclear graphite, University of Leeds, PhD thesis, 2002.

[32] S.L. Xu, H.W. Reinhardt, Determination of double-K criterion for crack propagation in quasi-brittle fracture, Part II: Analytical evaluating and practical measuring methods for three-point bending notched beams, Int J Fracture 98(2) (1999) 151-177.

[33] S. Xu, H.W. Reinhardt, A simplified method for determining double-K fracture parameters for three-point bending tests, Int J Fracture 104(2) (2000) 181-209.

[34] K. Park, G.H. Paulino, J.R. Roesler, Determination of the kink point in the bilinear softening model for concrete, Eng Fract Mech 75(13) (2008) 3806-3818.

[35] A. Tzelepi, P. Ramsay, A.G. Steer, J. Dinsdale-Potter, Measuring the fracture properties of irradiated reactor core graphite, J Nucl Mater 509 (2018) 667-678.

[36] RILEM, TC 50-FMC Fracture Mechanics of Concrete, Determination of the fracture energy of mortar and concrete by means of three-point bend tests on notched beams, Mater Struct 18(4) (1985) 287-290.

[37] P. Ouagne, G.B. Neighbour, B. Mcenaney, Crack growth resistance in nuclear graphites, Journal of Physics D Applied Physics 35(9) (2002) 927.

[38] R. Ince, Determination of the fracture parameters of the Double-K model using weight functions of split-tension specimens, Eng Fract Mech 96 (2012) 416-432.

[39] K.Y. Sze, H. Fan, C.L. Chow, Elimination of spurious pressure and kinematic modes in biquadratic 9-node plane element, Int J Numer Meth Eng 38(23) (1995) 3911-3932.

[40] Y.S. Jenq, S.P. Shah, Two parameter fracture model for concrete, Journal of Engineering Mechanics 111(10) (1985) 1227-1241.

[41] S. Kumar, S.R. Pandey, A.K.L. Srivastava, Determination of double-K fracture parameters of concrete using peak load method, Eng Fract Mech 131 (2014) 471-484.

[42] M. Elices, G.V. Guinea, J. Gomez, J. Planas, The cohesive zone model: advantages, limitations and challenges, Eng Fract Mech 69(2) (2002) 137-163.

[43] S.H. Kwon, Z. Zhao, S.P. Shah, Effect of specimen size on fracture energy and softening curve of concrete: part II. Inverse analysis and softening curve, Cement Concrete Res 38(8-9) (2008) 1061-1069.

[44] P.E. Roelfstra, F.H. Wittmann, Numerical method to link strain softening with failure of concrete, in: F.H. Wittmann (Ed.), Fracture Toughness and Fracture Energy of Concrete, Elsevier, Amsterdam, 1986, pp. 163-175.

[45] T. Oh-Oka, Y. Kitsutaka, K. Watanabe, Influence of short cut fiber mixing and curing time on the fracture parameters of concrete (in Japanese), Journal of Structural & Construction Engineering 65(529) (2000) 1-6.

[46] N. Nomura, H. Mihashi, M. Izumi, Correlation of fracture process zone and tension softening behavior in concrete, Cement Concrete Res 21(4) (1991) 545-550.

[47] K. Otsuka, H. Date, Fracture process zone in concrete tension specimen, Eng Fract Mech 65(2-3) (2000) 111-131.

[48] B. Allard, D. Rouby, G. Fantozzi, D. Dumas, P. Lacroix, Fracture behaviour of carbon materials, Carbon 29(3) (1991) 457-468.

[49] M. Sakai, J. Yoshimura, Y. Goto, M. Inagaki, R-curve behavior of a polycrystalline graphite - microcracking and grain bridging in the wake region, J Am Ceram Soc 71(8) (1988) 609-616.